Materials Advances

ROYAL SOCIETY OF CHEMISTRY

PAPER

View Article Online
View Journal | View Issue

Cite this: *Mater. Adv.*, 2026, 7, 577

Metal oxide hybrid materials: on-surface modulation of aggregation-induced fluorescence

Hannah Kurz, *[a] Florian Daumann, [ab] Jana Timm,[c] Tobias Seifert,[a] Phil Köhler, [c] Frank W. Heinemann, [d] Gerald Hörner, [ab] Roland Marschall *[c] and Birgit Weber *[ab]

Received 9th September 2025,
Accepted 14th November 2025

DOI: 10.1039/d5ma01035g

rsc.li/materials-advances

Covalent grafting of molecular compounds to extended oxide surfaces provides variable access to hybrid materials. While in many cases the properties of both components are additive, some favorable combinations can lead to the emergence of new properties. In this work, we report on the aggregation-induced fluorescence of an N_2O_2 (proto-) ligand **H_2L1** of the JÄGER-type on oxide surfaces. The ligand is non-fluorescent in solution but shows strong greenish-blue fluorescence in the bulk and, importantly, once covalently anchored to oxidic surfaces *via* an appended carboxylic acid moiety. Intermolecular π–π stacking interactions dominate the packing in single crystals both of **H_2L1** and a congener with methyl blocked acid function, **H_2L2**. As revealed by electronic spectroscopy, the high surface loadings of **H_2L1** on Al_2O_3 and TiO_2 allow stacking in a dense surface layer also on the solid supports. While non-fluorescent dilute solutions of **H_2L2** and **H_2L1** resonate only in the UV range below 380 nm, the consistent shift of the spectral onset to > 430 nm for bulk ligand and Al_2O_3-grafted material lends additional support to a supramolecular origin of fluorescence. Sharply reduced (but not vanishing) ligand fluorescence on TiO_2 indicates electron-injection to the conduction band to be operative, as further supported by the reduced emission lifetimes recorded *via* time-correlated single-photon counting. On-surface synthesis of the respective zinc(II) complexes likewise gives strongly fluorescent materials, showing again a reduced emission on TiO_2.

Introduction

Aggregation phenomena are well known to affect the optical properties of chromophores, as is perhaps best exemplified with the example of 'J-aggregates' and 'H-aggregates'. Both terms describe the phenomenon in which the aggregation of chromophores into a specific columnar arrangement strongly impacts their optical properties.[1] Here, aggregation serves to tune the energy and the width of an electronic transition, both in the absorption and the emission modes. In J-aggregates, the self-assembly leads to a bathochromic shift of the absorption bands,[2–4] while the complementary hypsochromic shift is observed for H-aggregates.[5,6] Especially, alteration of the emission properties through aggregation has gained a lot of attention in the last decade: Aggregation may induce quenching of the photoluminescence seen in the non-aggregated state (aggregation-caused quenching, ACQ), it might shift the emission energy as a function of the aggregation mode, and it might turn on the emission of an otherwise non-fluorescent chromophore (aggregation-induced emission, AIE).[7–11]

Aggregation phenomena are based on intermolecular supramolecular interactions such as hydrogen bonds, π–π stacking, or Van-der-Waals interactions that lead to a self-assembly of the respective molecules into larger, organized structures 'beyond molecules'. Another driving force for self-assembly are coordinative bonds, which furthermore enable the formation of sensor materials based on coordination-induced de-aggregation with optical response.[12–14]

Here, we present two Schiff base-like ligands that feature AIE behaviour. These ligands are fluorescent in the solid state, while non-fluorescent in solution. A similar optical behaviour was observed for the respective zinc(II) complex. As the ligand bears a carboxylic functional group in the ligand backbone, we immobilized the ligand and the zinc(II) complex on oxidic nanoparticles to investigate how 2D stacking on the oxidic surface affects the emission properties. We chose the TiO_2 modification anatase as a semiconducting material and Al_2O_3 as an isolating substrate to further investigate a possible

[a] *Inorganic Chemistry IV, University of Bayreuth, Universitätsstraße 30, 95447 Bayreuth, Germany. E-mail: Hannah.kurz@uni-bayreuth.de*
[b] *Institute for Inorganic and Analytical Chemistry, Friedrich Schiller University Jena, Humboldtstr. 8, 07743 Jena, Germany. E-mail: birgit.weber@uni-jena.de*
[c] *Physical Chemistry III, University of Bayreuth, Universitätsstraße 30, 95447 Bayreuth, Germany. E-mail: roland.marschall@uni-bayreuth.de*
[d] *Inorganic Chemistry, Friedrich-Alexander-University Erlangen-Nürnberg (FAU), Egerlandstraße 1, 91058 Erlangen, Germany*

electronic coupling of the adsorbate and the substrate. The findings indicate that aggregation-induced emission is also present in these hybrid materials, and that grafting onto TiO_2 results in emission quenching due to electronic interactions between the adsorbate and the substrate.

Results and discussion

Synthesis and characterization of the ligands and complexes

The ligand **H_2L1** was synthesized by a single-step condensation reaction between 3,4-diaminobenzoic acid and a keto-enol ether, as illustrated in Scheme 1. The tetradentate Schiff base-like ligand **H_2L1** bears a carboxylic acid group that can function as a surface anchoring group. For comparison with surface-grafted species, the reference ligand **H_2L2** with its carboxylic acid blocked as a methyl ester moiety was used. Purity and identity of the compounds were confirmed *via* ^{1}H-NMR spectroscopy, mass spectrometry, and elemental analysis, as shown in the supplementary information (SI) together with the experimental details. It is noted that reaction mixtures of the free acid ligand **H_2L1** and zinc(II) acetate gave no defined material.

Despite numerous trials, **[ZnL2(OH$_2$)]** did not yield crystals but consistently afforded as a thin and flexible 'hair-like' material. On the other hand, suitable material for single crystal X-ray structure analysis could be obtained from a slow evaporation setup at room temperature for **H_2L1** or directly from the isolated bulk material in the case of **H_2L2** (see Section 4 including Table S1 in the SI for crystallographic details). As a matter of fact, both compounds give rise to anisotropic stacking in the solid. The acid-appended N_2O_2 JÄGER-type ligand **H_2L1** crystallizes in the triclinic space group $P\bar{1}$. Different from the stoichiometry of the bulk material, the asymmetric unit contains a disordered ethanol molecule which is hydrogen-bonded to the carboxylic group of the ligand (Fig. S4 in the SI). Different from what is typically seen for carboxylic acids, no direct dimer formation *via* an eight-membered cyclic H-bonded motif is present in **H_2L1**. Instead, two ethanol molecules serve as a spacer between adjacent molecules to form a twelve-membered hydrogen-bonded motif comprising O2–H2···O9–H9···O1 linkages, including both carbonyl and hydroxylic oxygens of the anchoring group (Fig. 1). This finding supports the expected ability of the ligand to interact with hydroxylic surfaces *via* two anchoring points. It is noted that while all parts of the ligand are engaged in supramolecular stacking with neighbouring molecules (see Fig. S5, SI), the two chelate arms behave differently. The arm located *para* to the methyl ester retains co-planarity to the phenylene backbone, what allows 'head-to-tail' stacking of these planar moieties in columns of *ca.* 3.5 Å spacing along lattice vector ***a***. The second arm, located in the meta position is rotated from co-planarity with the phenylene backbone.

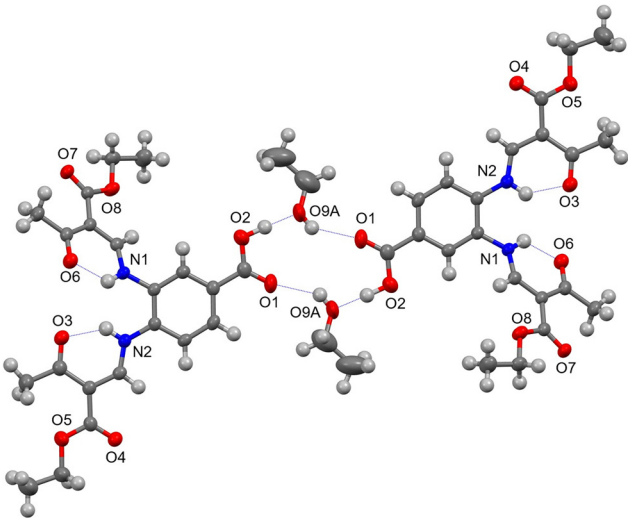

Fig. 1 Molecular structure of supramolecular dimers of **H_2L1**·EtOH in the crystal. For clarity only the EtOH molecule with the higher site occupancy is shown. Displacement ellipsoids are given at 50% probability. Hydrogen atoms are illustrated as spheres of arbitrary size. Colour code: carbon (grey), oxygen (red), nitrogen (blue), hydrogen (light grey). Hydrogen bonds are illustrated as blue dashed lines.

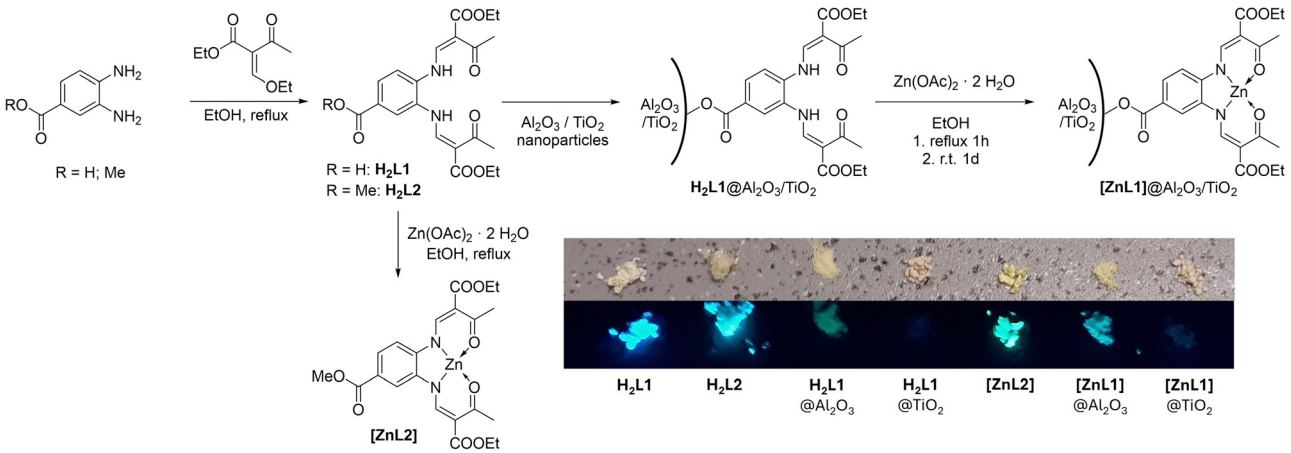

Scheme 1 Synthetic route to the ligands **H_2L1** and **H_2L2**, reference zinc complex **[ZnL2]** and immobilization of ligand/complex on oxidic surfaces. Appearance and UV response of the synthesized compounds and hybrid materials (λ_{exc} = 365 nm).

For comparison, the molecular structure of the reference ligand **H_2L2** is given in Fig. S6 and S7 the SI. **H_2L2** crystallizes in the monoclinic space group *P*21/*c* with two crystallographically independent but structurally very similar molecules in the asymmetric unit. Different from the above case, packing of **H_2L2** infers out-of-plane rotation of both chelate arms, giving rise to helical arrangements of the scissor-like molecules along lattice axis *b* (Fig. S8 in the SI). As expected, the metrics of the N_2O_2 chelate site in both compounds are only marginally affected by the nature of the remote substituent, –H *vs.* –Me (supported by DFT modelling, see Section 5 including Table S2, SI). This notion is further supported by the similarity of the ^{1}H-NMR spectra in $CDCl_3$ (see Fig. S1–S3, SI). Accordingly, the synthetically accessible **[ZnL2]** is a valid model for the elusive complex **[ZnL1]**, which cannot be directly derived from **H_2L1** but only forms on the surface as discussed in the next paragraph.

Synthesis of hybrid materials

The hybrid materials were synthesized in two steps, as shown in Scheme 1. To avoid metal complexation *via* the carboxylic group, the ligand was anchored on the substrate prior to complex formation. Immediate light-yellow coloring of the Al_2O_3/TiO_2 powders was visible in ethanolic suspension, indicating the deposition of the ligand on the surface. Nonbound ligand was removed from the samples by washing the powder three times with ethanol until a colourless supernatant was obtained after centrifugation. Subsequent reaction with zinc(II) acetate dihydrate results in pale yellow **[ZnL1]**@Al_2O_3/TiO_2.

Elemental analysis of the composite materials gives evidence of extensive surface grafting, in particular, the large carbon contents between 3.5 and 6.0 weight % indicate high surface density of the adsorbed ligands/complex (Table 1). As the ligand is the only carbon and nitrogen source in **H_2L1**@Al_2O_3 and **H_2L1**@TiO_2, the C : N ratio of the ligand directly translates to the C : N ratio expected for the hybrid materials. Indeed, this ratio does not change significantly after immobilization of the ligand, indicating that the ligand stays intact on the surface. The same applies for the zinc complexes on TiO_2 and Al_2O_3. Furthermore, elemental analysis gives an estimate of the amount of immobilized ligand/complex in the hybrid materials, thereby providing an indication of the surface coverage; details are given in Section S6 in the SI. Two observations are essential. First, the molar percentage of ligand/complex is large on both oxide carriers. Second, the on-surface synthesis step of the complex in an ethanol suspension leaves coverage largely unaffected. A slight leakage is obtained during synthesis of **[ZnL1]**@TiO_2, reducing the molar percentage from 8.5% to 7.1%, while the respective values obtained on Al_2O_3 are essentially identical within experimental error (10.3% *versus* 10.9%). This is remarkable, as it indicates strong surface binding which presumably goes beyond dispersion forces and/or hydrogen bonding. The quantity of **H_2L1** and **[ZnL1]** on the surface of the substrates and the homogeneity of this immobilization on the surface were further investigated by scanning electron microscopy-energy dispersive X-ray spectroscopy (SEM-EDS) maps and X-ray photoelectron spectroscopy (XPS). In both cases, particle agglomerates with different sizes are visible in the SEM images, while the agglomerates of Al_2O_3 are in the range of 10 to 30 μm and TiO_2 below 5 μm (Fig. S14). The morphology of the materials due to the immobilization of **H_2L1** and **[ZnL1]** could be perceived. After immobilization, the morphology of the materials remains, and the agglomerate sizes are in the same ranges as in the bare substrates. Further, the elemental composition was probed by SEM-EDS and XPS (XPS survey scans see Fig. S15). In Table S3 the results of XPS and SEM-EDS are listed and show slight differences, which could be explained by the different sensitivities for surfaces of materials and penetration depth of the methods. Furthermore, quantifying light elements *via* EDS is very difficult due to poor sensitivity. The XPS values of the materials are therefore more reliable. The comparison of the XPS values and values of the elemental analysis (*cf.* Table 1) shows the almost doubled amount for carbon and nitrogen. This effect is attributed to the solely surface sensitivity of XPS, as expected the concentration of **H_2L1** and **[ZnL1]** is higher on the surface than in the bulk of the agglomerates. Due to agglomerate formation, some immobilized molecules could be enclosed in the voids between the particles. Further, XPS data reveals the amount of zinc on the surface of the materials. Here, values of 1.8 and 3.5% are reached, underlining the trend of complex formation on the surface of the materials. Additionally, to prove the homogeneity of the hybrid materials SEM-EDS mapping (Fig. S16) was performed. Here, the homogenous distribution of **[ZnL1]** on the surface of the substrates TiO_2 and Al_2O_3 could be confirmed. The IR analysis of the hybrid materials indicates covalent binding *via* the carboxylate function (see Scheme 1). In keeping with this binding hypothesis, the generally larger loading on Al_2O_3 may hint at a slightly higher amount of accessible hydroxylic oxide groups in Al_2O_3 compared to TiO_2. This may be due to differences in surface area, morphology, or the surface hydration from the synthesis of the materials or a combination thereof.

Table 1 Elemental analysis of the different compounds. The theoretical values are given in brackets

Compound	C/%	H/%	N/%	Ratio C : N
H_2L1	58.28 [58.33]	5.58 [5.59]	6.42 [6.48]	9.1 : 1 [9.0 : 1]
[ZnL2] + H_2O	49.44 [49.04]	5.05 [4.71]	5.01 [5.45]	9.9 : 1 [9.0 : 1]
H_2L1@Al_2O_3	6.03	0.99	0.68	8.9 : 1
[ZnL1]@Al_2O_3	5.37	0.97	0.48	11.2 : 1
H_2L1@TiO_2	4.94	0.67	0.56	8.8 : 1
[ZnL1]@TiO_2	3.50	0.49	0.38	9.2 : 1

The hybrid materials were further characterized using diffuse reflectance infrared Fourier transform (DRIFT) spectroscopy (Fig. 2 and Fig. S17 in the SI for **H_2L1** and S18 for **[ZnL1]** compounds). The pristine oxides exhibit characteristic Al–O/Ti–O bands in the fingerprint region from 700 cm^{-1} to 1300 cm^{-1}. Additionally, for both oxides, the deformation vibration of surface water is visible at around 1600 cm^{-1}. In contrast to TiO_2, for the Al_2O_3 carrier, additional weak bands from 1300 cm^{-1} to 1600 cm^{-1} are visible and can be assigned to adsorbed carbonates.[15]

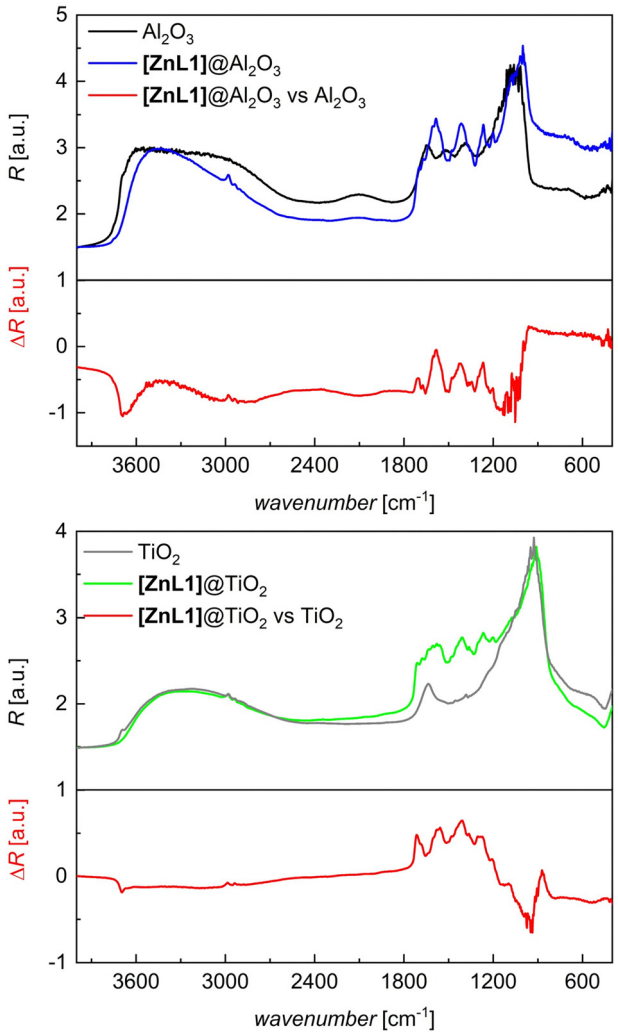

Fig. 2 DRIFT spectra of the substrates TiO_2 (grey) and Al_2O_3 (black), the immobilized complex **[ZnL1]** (blue, green) and the difference spectra (red).

A broad band due to surface OH stretching vibrations and hydrogen-bonded water molecules dominates the region between 3000 and 3800 cm^{-1}. A weak shoulder on the high-energy tailing at around 3700 cm^{-1} is indicative of isolated surface OH-groups. Both, **H_2L1** and **[ZnL1]** show the expected high number of sharp bands in the fingerprint range from 1000 cm^{-1} to 1800 cm^{-1}. While many of these vibrations are preserved in the hybrid material, confirming an intact ligand/complex, we note the absence of some modes, what becomes evident as negative peaks in difference spectra (red in Fig. 2). For instance, the band corresponding to isolated surface OH-groups at 3700 cm^{-1} is absent after immobilization, confirming the interaction of the ligand with the surface hydroxy groups. Clearly, this feature is more pronounced in the Al_2O_3 difference spectra at 3700 cm^{-1} compared to TiO_2. This finding is consistent with the elemental analysis data and supports better availability of isolated surface hydroxy groups and interaction thereof with the ligand/complex *via* the anchoring group on Al_2O_3.

The diagnostic carbonyl modes of carboxylic acids are sensitive probes of the mode of surface grafting.[16] Accordingly, adsorption of carboxyl-appended dyes on Al_2O_3 and TiO_2 is typically followed *via* the IR response of the carbonyl moieties.[17,18] In our samples the overlap of carbonyl modes due to the presence of several carbonyl moieties in the chelate cycle and the anchor itself impedes a similarly conclusive analysis of the spectral region between 1500 and 1700 cm^{-1}. While we therefore refrain from drawing definite conclusions on the (dominant) binding modes of the carboxylic acid anchor on the surface, clearly, the pattern in the high-energy envelope around 1700 cm^{-1} is different for Al_2O_3 and TiO_2-based samples. We conclude that significantly less 'free' carbonyls can be probed on Al_2O_3 than on TiO_2, eventually supporting different adsorption modes on both surfaces. This notion is supported by DFT-based computation of vibration spectra on truncated surface models (see Section S5 in the SI). As shown in Fig. S19 (top left and top right; SI), the vibration spectrum of **H_2L1**/**[ZnL1]**@Al_2O_3 is convincingly matched by the theoretical model, when an adsorption mode *via* binuclear anchoring is assumed. No such agreement is observed for the TiO_2 models, hinting towards a more complex or mixed coordination mode (Fig. S19, bottom left and right). Further analysis of the hybrid materials was conducted to assess their integrity after hybrid formation. The powder X-ray diffraction (PXRD) data in Fig. S20 show that during the immobilization of the **H_2L1** and **[ZnL1]**, no structural changes of the support materials TiO_2 and Al_2O_3 proceed. In the PXRD data of **[ZnL1]**@Al_2O_3 reflections with low intensity appear. These additional reflections result from the immobilization of the complex on the Al_2O_3 (see PXRD data in Fig. S20).

Optical characterization

The optical properties of **H_2L1**, **H_2L2** and **[ZnL2(OH$_2$)]** were studied in the non-coordinating solvent $CHCl_3$, as zinc(II) complexes of JÄGER-type ligands are well-known for their tendency to aggregate in non-coordinating solvents, eventually affecting absorption and emission (see Fig. 3).[12,14] We also recorded spectra in the coordinating solvent pyridine, in which aggregation is inhibited (see Fig. S21, SI). The ligands **H_2L1** and **H_2L2** show very similar absorption spectra composed of two strong absorption bands below 400 nm in both solvents ($\lambda_{max,1} \approx 309$ nm, $\varepsilon_{max,1} \approx 35.000$ $lmol^{-1}$ cm^{-1}; $\lambda_{max,2} \approx 357$ nm, $\varepsilon_{max,2} \approx 29.000$ $lmol^{-1}$ cm^{-1}; details see Table S4 in the SI). Coordination with zinc(II) in $CHCl_3$ solution leads to a bathochromic shift of both bands and a distinct decrease of the extinction coefficient ($\lambda_{max,1} \approx 333$ nm, $\varepsilon_{max,1,CHCl_3} \approx 29.500$ $lmol^{-1}$ cm^{-1}, $\varepsilon_{max,1,pyridine} \approx 37.000$ $lmol^{-1}$ cm^{-1}; $\lambda_{max,2} \approx 390$ nm, $\varepsilon_{max,2,CHCl_3} \approx 21.000$ $lmol^{-1}$ cm^{-1}, $\varepsilon_{max,2,pyridine} \approx 27.500$ $lmol^{-1}$ cm^{-1}). While the spectral appearance is very similar in pyridine solution, we noted that the extinction coefficients are significantly larger. All samples are (nearly) non-emissive in solution (photographs of the UV irradiated solutions and emission spectra are shown in Fig. 3 and Fig. S21, emission spectra are shown in Fig. S22 in the SI). While no signals were obtained for the ligands and **[ZnL2]** in

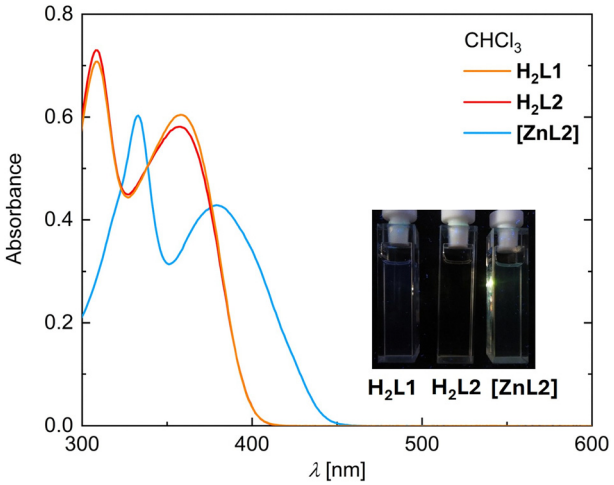

Fig. 3 UV-vis spectra recorded of **H_2L1** (orange), **H_2L2** (red), and of the zinc(II) reference complex **[ZnL2]** (blue) in $CHCl_3$ solutions ($c_0 \approx 3 \times 10^{-5}$ M). Inset: Photo of the solutions under UV irradiation (λ_{exc} = 365 nm).

$CHCl_3$, **[ZnL2]** in pyridine shows emission, though very weak and barely distinguishable from the background noise.

The UV absorption of the bulk solid compounds largely echoes the properties of the isolated molecules in dilute solutions (Fig. 4 and Fig. S23). Accordingly, diffuse reflectance spectra of **H_2L1** and **[ZnL2]** show a broad absorption band in the UV range. However, the spectral range of strong absorption extends to 410 nm for the reference ligand **H_2L2**, that is, towards the visible regime (see Fig. 4 and Fig. S24 (left) for normalized spectra), whereas for **[ZnL2]** we see an extended absorption up to 430 nm (see Fig. S23 and Fig. S24 (right) in the SI for normalized spectra). We conclude that aggregation in the solid state results in a significant extension of the absorption range into the visible regime. This effect, if more moderate, persists in the hybrid materials. Notably, the long-wavelength extensions are more pronounced for **H_2L1**@Al_2O_3/**[ZnL1]**@Al_2O_3 with an isolating substrate than for **H_2L1**@TiO_2/**[ZnL1]**@TiO_2 with its semiconducting substrate, respectively. We thus take the spectral extension as a hint of aggregation in the hybrid materials.

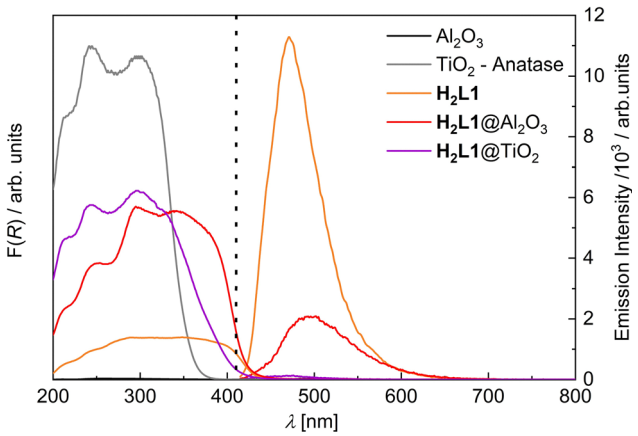

Fig. 4 Diffuse reflectance spectra (Kubelka–Munk analysis, left) and photoluminescence spectra (right) of bulk **H_2L1**, the neat substrates TiO_2 and Al_2O_3, and the hybrid materials. Dashed line represents the excitation wavelength of 410 nm for the PL experiments.

The effect of aggregation on the emission behaviour is even more pronounced. Both ligands, **H_2L1** and **H_2L2** and the zinc complex **[ZnL2]** are essentially non-emissive in solution, whereas the bulk materials show a strong blue/green emission as visualized in Scheme 1. Interestingly, the Al_2O_3 hybrid materials are also emissive, indicating a turn-on emission effect due to immobilization. Any emission of the hybrid material must be based on excitation of the **H_2L1** and **[ZnL1]** chromophores, as both show absorption at 410 nm, and both parent TiO_2 and Al_2O_3 are silent. The spectra (Fig. 4 and Fig. S23 in the SI) thus give quantitative support to the qualitative visual impression of the irradiated solids in Scheme 1.

The neat compounds **H_2L1** and **[ZnL2]** show the strongest emission. Compared to the pristine materials, the emission intensity of the Al_2O_3 hybrid materials is generally reduced but spectrally conserved. These aspects may hint to either or both effects of dilution of the fluorophores on the oxide surfaces or the more general difference between 3D stacking in the neat compounds and 2D stacking on the surface. It should be noted that the Al_2O_3 hybrid materials are composed of only approximately 11% ligand/complex (see discussion on elemental analysis and Table 1).

Effects of packing density on the emission are well established.[8,19–22] Steric differences in surface stacking may also account for the diverting shifts of the emission maxima with respect to the pristine materials. While the peak position undergoes a bathochromic shift by $\Delta E \approx -700$ cm^{-1} for the ligand ($\lambda_{em,max}$ (**H_2L1**@Al_2O_3) = 486 nm) the opposite is true for the zinc complex ($\lambda_{em,max}$ (**[ZnL1]**@Al_2O_3) = 481 nm), which is shifted hypsochromically by $\Delta E \approx +1200$ cm^{-1}.

Overall, the TiO_2 hybrids are less emissive. While the amount of immobilized **H_2L1**/**[ZnL1]** is certainly smaller in the TiO_2 hybrid materials compared to the Al_2O_3 hybrid materials, the drastic decrease in photoluminescence (PL) intensity cannot solely be explained by dilution effects but rather indicates additional effects. One might be the electronic impact of the substrate (Al_2O_3: insulator; TiO_2: semiconductor) and electronic interactions between **H_2L1**/**[ZnL1]** and TiO_2. In particular, the conduction band of TiO_2 is known to provide a valid pathway for electron-transfer quenching in a sensitization scenario.[23,24]

PL lifetimes, which probe the excited ligand/complex, were recorded at the respective emission maxima. Two excitation wavelengths were chosen to allow either selective excitation of the adsorbate (λ_{exc} = 404 nm) or excitation of the entire electronic system (λ_{exc} = 355 nm), which includes band gap excitation of TiO_2. Table 2 summarizes PL lifetimes with λ_{exc} = 404 nm (see Table S5 for PL lifetimes and Fig. S25; for time-correlated single photon counting (TCSPC) spectra with λ_{exc} = 355 nm, Fig. S26). Overall, the results from both excitation channels are in good agreement. This once again emphasises that the excitation of the chromophore is decisive for the changes in PL emission. The lifetime decays could be fitted best with biexponential functions. For all samples, the shorter lifetime τ_2 is the main component.

Table 2 Photoluminescence (PL) lifetimes in ns (λ_{exc} = 404 nm) and amplitudes of the biexponential fit components recorded at the respective maximum detection wavelengths

Compound	τ_1/ns	τ_2/ns
H_2L1 (470 nm)	1.69 (45.4%)	0.88 (54.6%)
H_2L1@Al_2O_3 (486 nm)	2.49 (18.7%)	0.46 (81.3%)
H_2L1@TiO_2 (442 nm)	1.31 (0.3%)	0.18 (99.7%)
[ZnL2] (500 nm)	1.38 (17.1%)	0.59 (82.9%)
[ZnL1]@Al_2O_3 (481 nm)	1.43 (31.4%)	0.36 (68.6%)
[ZnL1]@TiO_2 (487 nm)	1.18 (23.1%)	0.26 (76.9%)

Indeed, the excited-state decays recorded for the bulk ligand **H_2L1** and its immobilized forms reflect the qualitative order of emission intensities given in Fig. 5. In line with the reduced emission intensity, rapid decay prevails for both hybrid materials, whereas the bulk ligand shows more sustained emission. The decay curves could be fitted to biexponential models for **H_2L1** and **H_2L1**@Al_2O_3, with the longer-lived component significantly quenched in the latter (Fig. 5). For related organic compounds in solution, biexponential decays can be attributed to distinct states.[25,26] However, this attribution is not feasible for heterogeneous compounds due to their inherent site heterogeneity.[27,28] In the case of **H_2L1**@TiO_2, the longer lifetime is nearly completely quenched, resulting in essentially single-exponential decay.

Intriguingly, the quenching effect of surface grafting is less expressed for the zinc complex, particularly on TiO_2 (see Fig. S25 and Table 2). Quite different from the ligand on TiO_2, significant emission is still observed for **[ZnL1]**@TiO_2, concomitant with a nanosecond-lived kinetic component, which hardly differs from those in the bulk complex and **[ZnL1]**@Al_2O_3. We cannot present a fully satisfying explanation of these differences between **H_2L1**@TiO_2 and **[ZnL1]**@TiO_2. Electron injection from the excited adsorbate to TiO_2 *via* a sensitization mechanism must be expected to be equally viable dissipation pathways for both adsorbates. Indeed, an estimation of the excited-state redox potentials with DFT tools indicates highly exergonic charge injection after excitation of both, **H_2L1**@TiO_2 and **[ZnL1]**@TiO_2 (Scheme S1 in the SI, see Section S1, SI, for full details).

The complementary process, that is, hole transfer from TiO_2 to the adsorbate, must be expected to affect the dynamics of electron/hole pairs after band-gap excitation. Given the relative positions of the valence band and the adsorbate donor potential (Scheme S1 in the SI), such processes are likewise viable. Lifetimes of the residual conduction-band electrons were extracted from nanosecond transient absorption (TA) spectra in the NIR regime after band gap excitation at λ_{exc} = 355 nm of TiO_2, **H_2L1**@TiO_2 and **[ZnL1]**@TiO_2. Spectra shown in Fig. S27, SI, are very similar at first glance and feature signals in the range between 760 nm and 950 nm, in which range a convolution with the emission signal of the adsorbate can be excluded. These transient absorption spectroscopy (TAS) signals are assigned as the response of photogenerated electrons according to the literature.[29–33] The observed slight shift in the absorption maximum of these photogenerated electrons suggests interactions between **H_2L1**/**[ZnL1]** and semiconducting TiO_2. Therefore, a subtle change in the electronic structure of TiO_2 is presumed due to immobilization of **H_2L1**/**[ZnL1]** on TiO_2.

The lifetimes of the charge carriers at the different absorption wavelengths could further underline these interactions. Here, the TA signals at 780 and 840 nm were analysed due to the observed changes in intensity when comparing the TA spectra of the different materials (Fig. S27, SI). In Fig. S28, SI, the measured decays are presented, while in Table 3, the resulting lifetimes are listed. For all materials, a biexponential decay is present. The lifetime of charge carriers of the used TiO_2 modification, anatase, is described to be in the µs range.[31] In the present case, τ_1 is shorter than described in the literature. Also, the shorter-lived electrons (τ_2) were observed in the literature before.[29,30] For the lifetimes of the photogenerated electrons, different trends regarding the different hybrids are evident. When probing the lifetime at 780 nm, the long-lived electrons reach lifetimes up to 427 ns in **H_2L1**@TiO_2, while the electrons in TiO_2 surprisingly only exhibit a lifetime of 182 ns. The opposite behaviour could be observed when probing at 840 nm; here, the long-lived electrons of TiO_2 exhibit the longest lifetime of 473 ns, while the long-lived electrons in **H_2L1**@TiO_2 live only for 261 ns. This effect underscores that the ligand on the surface of TiO_2 interacts with the TiO_2's electrons, thereby prolonging or shortening their lifetimes. In the case of **[ZnL1]**@TiO_2, there is no such clear trend visible. Thus, the lifetimes of the long-lived electrons in **[ZnL1]**@TiO_2 are comparable at the different probe wavelengths with 363 ns

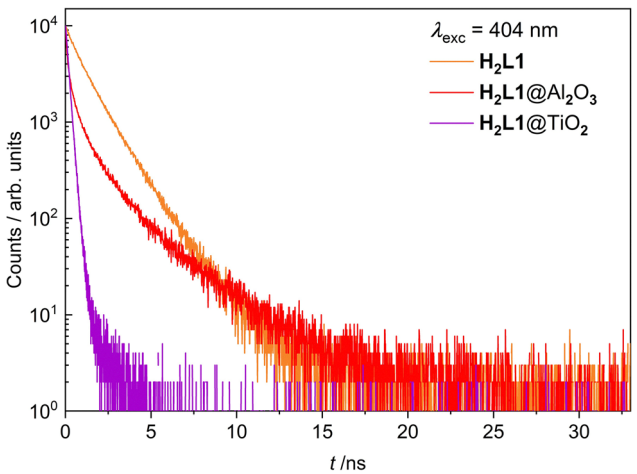

Fig. 5 TCSPC decay of the bulk **H_2L1**, and the **H_2L1** hybrid materials (λ_{exc} = 404 nm).

Table 3 ns-TAS lifetimes of the TiO_2 and the TiO_2 based hybrid materials at different probe (absorption) wavelengths in ns (λ_{exc} = 355 nm)

Compound	λ_{probe}/nm	τ_1/ns	τ_2/ns
TiO_2	780	182	9
	840	473	16
H_2L1@TiO_2	780	427	14
	840	261	11
[ZnL1]@TiO_2	780	363	6
	840	454	11

(at 780 nm) and 454 ns (840 nm). Hence, the immobilization of the complex on the TiO_2 surface leads to a slight stabilization of the electrons in TiO_2, and the presence of electronic interaction of the semiconductor TiO_2 and **H_2L1** or **[ZnL1]** was further emphasized by TAS investigations.

Conclusion

The novel tetradentate ligands **H_2L1** and **H_2L2** and the respective zinc(II) complex **[ZnL2]** have been reported, both showing no emission in the solution state, but a strong emission upon aggregation in the solid state. The carboxylate functional group in the ligand backbone enables the covalent anchoring of **H_2L1** or **[ZnL1]** on metal oxide surfaces. While the Al_2O_3 hybrid materials are highly emissive, grafting of **H_2L1**/**[ZnL1]** on TiO_2 results in hybrid materials with a drastically reduced emission. The sole observation of emission of the hybrid materials is striking, as this suggests that the ligand or zinc(II) complex is present on the surfaces in an aggregated manner. On the other hand, the type of substrate, insulator Al_2O_3 or semiconductor TiO_2, has a significant impact on the emission of these hybrid materials. In particular, the ligand **H_2L1** shows strongly reduced lifetimes on TiO_2, hinting towards emission quenching *via* electronic coupling between the ligand and TiO_2. This effect is less pronounced for the **[ZnL1]** hybrid material. These properties are also reflected in the TAS characterization, which underlines the electronic interaction between **H_2L1** and TiO_2, and the much weaker coupling for **[ZnL1]**@TiO_2.

Conflicts of interest

There are no conflicts to declare.

Data availability

The data supporting this article have been included as part of the supplementary information (SI). Supplementary information is available. See DOI: https://doi.org/10.1039/d5ma01035g.

CCDC 2484339 (**H_2L1**) and 2481395 (**H_2L2**) contain the supplementary crystallographic data for this paper.[34a,b]

Acknowledgements

We gratefully acknowledge the support and funding by the German Research Foundation (DFG), project numbers 463161096, 509879467, and within CRC 1585 'Structured functional materials for multiple transport in nanoscale confinements' (project number 492723217) for subproject B02. We thank the Northern Bavarian NMR Centre and the Central Analytics of the Department of Chemistry for analytical measurements. We thank Dr Anja Hofmann for the introduction to the solid-state UV-Vis spectrometer, Kevin Ries for SEM-EDS analysis and Lion Schumacher for XPS data analysis. The authors also thank the Bavarian Polymer Institute (BPI, Keylab Electron and Optical Microscopy) for the opportunity to use the SEM Zeiss Leo 1530 and the XPS device. R. M. acknowledges funding by the DFG in the Major Research Instrumentation funding program, project INST 91/459-1 (project no. 468685973).

Notes and references

1 N. J. Hestand and F. C. Spano, *Chem. Rev.*, 2018, **118**, 7069–7163.
2 J. H. Kim, T. Schembri, D. Bialas, M. Stolte and F. Würthner, *Adv. Mater.*, 2022, **34**, 2104678.
3 S. B. Anantharaman, J. Kohlbrecher, G. Rainò, S. Yakunin, T. Stöferle, J. Patel, M. Kovalenko, R. F. Mahrt, F. A. Nüesch and J. Heier, *Adv. Sci.*, 2021, **8**, 1903080.
4 F. Würthner, T. E. Kaiser and C. R. Saha-Möller, *Angew. Chem., Int. Ed.*, 2011, **50**, 3376–3410.
5 A. T. Haedler, K. Kreger, A. Issac, B. Wittmann, M. Kivala, N. Hammer, J. Köhler, H.-W. Schmidt and R. Hildner, *Nature*, 2015, **523**, 196–199.
6 Z. Li, Y. Xiang, J. Li, L. Feng, M. Zhang, Z. Zhang, S. Yan and B. Xu, *Angew. Chem.*, 2025, **137**, e202413986.
7 S.-Y. Yang, Y. Chen, R. T. K. Kwok, J. W. Y. Lam and B. Z. Tang, *Chem. Soc. Rev.*, 2024, **53**, 5366–5393.
8 J. Mei, Y. Hong, J. W. Y. Lam, A. Qin, Y. Tang and B. Z. Tang, *Adv. Mater.*, 2014, **26**, 5429–5479.
9 Y. Liu, L. Wang, L. Xu and Y. Song, *J. Mater. Chem. C*, 2023, **11**, 13403–13417.
10 M. Gao and B. Z. Tang, *ACS Sens.*, 2017, **2**, 1382–1399.
11 J. Mei, N. L. C. Leung, R. T. K. Kwok, J. W. Y. Lam and B. Z. Tang, *Chem. Rev.*, 2015, **115**, 11718–11940.
12 S. Di Bella, *Dalton Trans.*, 2021, **50**, 6050–6063.
13 J. K.-H. Hui, Z. Yu, T. Mirfakhrai and M. J. MacLachlan, *Chem. – Eur. J.*, 2009, **15**, 13456–13465.
14 H. Kurz, G. Hörner, O. Weser, G. Li Manni and B. Weber, *Chem. – Eur. J.*, 2021, **27**, 15159–15171.
15 C. Weilach, C. Spiel, K. Föttinger and G. Rupprechter, *Surf. Sci.*, 2011, **605**, 1503–1509.
16 S. Tunesi and M. A. Anderson, *Langmuir*, 1992, **8**, 487–495.
17 K. Vinodgopal, X. Hua, R. L. Dahlgren, A. G. Lappin, L. K. Patterson and P. V. Kamat, *J. Phys. Chem.*, 1995, **99**, 10883–10889.
18 J. Fujisawa, S. Kato and M. Hanaya, *J. Phys. Chem. C*, 2021, **125**, 25075–25086.
19 S. Sarkar, B. Kanchibotla, J. D. Nelson, J. D. Edwards, J. Anderson, G. C. Tepper and S. Bandyopadhyay, *Nano Lett.*, 2014, **14**, 5973–5978.
20 H. Tong, Y. Dong, Y. Hong, M. Häussler, J. W. Y. Lam, H. H.-Y. Sung, X. Yu, J. Sun, I. D. Williams, H. S. Kwok and B. Z. Tang, *J. Phys. Chem. C*, 2007, **111**, 2287–2294.
21 Z. Zhao, H. Zhang, J. W. Y. Lam and B. Z. Tang, *Angew. Chem., Int. Ed.*, 2020, **59**, 9888–9907.
22 J. Kuwabara, Y. Ogawa, A. Taketoshi and T. Kanbara, *J. Organomat. Chem.*, 2011, **696**, 1289–1293.
23 W. Macyk, K. Szaciłowski, G. Stochel, M. Buchalska, J. Kuncewicz and P. Łabuz, *Coord. Chem. Rev.*, 2010, **254**, 2687–2701.

24 W. Macyk, G. Stochel and K. Szaciłowski, *Chem. – Eur. J.*, 2007, **13**, 5676–5687.
25 W. Rodríguez-Córdoba, J. S. Zugazagoitia, E. Collado-Fregoso and J. Peon, *J. Phys. Chem. A*, 2007, **111**, 6241–6247.
26 S. Husain, N. Pandey, N. Fatma, S. Pant and M. S. Mehata, *J. Mol. Liq.*, 2022, **368**, 120783.
27 A. Habti, D. Keravis, P. Levitz and H. Van Damme, *J. Chem. Soc., Faraday Trans. 2*, 1984, **80**, 67.
28 H. Wang and J. M. Harris, *J. Phys. Chem.*, 1995, **99**, 16999–17009.
29 J. Schneider, M. Matsuoka, M. Takeuchi, J. Zhang, Y. Horiuchi, M. Anpo and D. W. Bahnemann, *Chem. Rev.*, 2014, **114**, 9919–9986.
30 J. Tang, J. R. Durrant and D. R. Klug, *J. Am. Chem. Soc.*, 2008, **130**, 13885–13891.
31 A. Kafizas, X. Wang, S. R. Pendlebury, P. Barnes, M. Ling, C. Sotelo-Vazquez, R. Quesada-Cabrera, C. Li, I. P. Parkin and J. R. Durrant, *J. Phys. Chem. A*, 2016, **120**, 715–723.
32 X. Wang, A. Kafizas, X. Li, S. J. A. Moniz, P. J. T. Reardon, J. Tang, I. P. Parkin and J. R. Durrant, *J. Phys. Chem. C*, 2015, **119**, 10439–10447.
33 A. Kafizas, Y. Ma, E. Pastor, S. R. Pendlebury, C. Mesa, L. Francàs, F. Le Formal, N. Noor, M. Ling, C. Sotelo-Vazquez, C. J. Carmalt, I. P. Parkin and J. R. Durrant, *ACS Catal.*, 2017, **7**, 4896–4903.
34 (*a*) CCDC 2484339: Experimental Crystal Structure Determination, 2025, DOI: **10.5517/ccdc.csd.cc2pd4z7**; (*b*) CCDC 2481395: Experimental Crystal Structure Determination, 2025, DOI: **10.5517/ccdc.csd.cc2p9304**.